GEOPHYSICS, VOL. 89, NO. 3 (MAY-JUNE 2024); P. S251–S265, 25 FIGS.
10.1190/GEO2023-0354.1

DOI:10.1190/geo2023-0354.1

Strain field reconstruction from helical-winding fiber distributed acoustic sensing and its application in anisotropic elastic reverse time migration

Lele Zhang[1], Yang Zhao[1], Lu Liu[2], Fenglin Niu[3], Wei Wu[4], Chuangyang Wang[1], Hengyu Tang[5], Jingming Li[6], Jiahui Zuo[1], Yi Yao[7], and Yixin Wang[2]

ABSTRACT

Optical fiber-based distributed acoustic sensing (DAS) technology has been a popular seismic acquisition tool due to its easy deployment, wide bandwidth, and dense sampling. However, the sensitivity of straight optical fiber to only single-axis strain presents challenges in fully characterizing multicomponent seismic wavefields, making it difficult to use these data in elastic reverse time migration (ERTM). The helical-winding fiber receives projecting signals projected onto the fiber from all seismic strain field components and has the potential to reconstruct those strain components for ERTM imaging. Here, we give detailed mathematical principles of helical fiber-based DAS with crucial parameters such as pitch angle, gauge length, and rotating angle. At least six points of DAS responses are required in one or several winding periods to rebuild the strain fields within the seismic wavelength. The projecting matrix of conventional regular helical-winding fiber is singular and ill conditioned, which results in computation challenges for the inverse of the Hessian matrix for strain component reconstruction. To tackle this problem, we develop a nonregular variant pitch-angle winding configuration for helical fiber. Our winding design is validated using the rank and condition number of the projecting matrix, which is proven to be an important tool in the reconstruction of the original seismic strains. The recovered strain components from the DAS response are then used to backward propagate the receiver wavefields in ERTM with an efficient P/S decoupled approach. To summarize, we develop a novel winding design of helical fiber to recover the strain fields and then develop an efficient 3D anisotropic P/S wave-mode decomposition method for generating vector P and S wavefields during their propagation. Both methods are applied to build an anisotropic DAS-ERTM workflow for producing PP and PS images. Two synthetic examples demonstrate the effectiveness of our approach.

INTRODUCTION

Elastic reverse time migration (ERTM) exhibits a promising ability in sweet point detection (Caldwell, 1999; Granli et al., 1999; Zhao et al., 2018; Liu, 2019) and complex structure investigation (Tang et al., 2009). Up to the present, ERTM has been widely applied to anisotropic media such as vertical transverse isotropic (VTI) and tilted transversely isotropic (TTI) media, which result in better images than those of isotropic approaches (Yang et al., 2019; Zhang et al., 2022; Zuo et al., 2022). Anisotropic ERTM usually consists of three steps: source and receiver wavefield modeling, P/S wave-mode decomposition, and applying elastic imaging conditions. The imaging condition directly determines the image quality of ERTM, which correlates quasi P- (qP-) and quasi S- (qS-) wavefields at the zero-time lag. Therefore, a key point for ERTM is to separate P/S wave modes during their propagation. In aniso-

Manuscript received by the Editor 11 June 2023; revised manuscript received 20 January 2024; published ahead of production 16 February 2024; published online 17 April 2024.
[1]China University of Petroleum (Beijing), National Key Laboratory of Petroleum Resources and Engineering, Beijing, China and China University of Petroleum (Beijing), Unconventional Petroleum Research Institute, Beijing, China. E-mail: cup_lele@163.com; zhaoyangprof1@qq.com (corresponding author); wangcy0y@163.com; zuojiahui_2007@126.com.
[2]Aramco Research Center-Beijing, Aramco Asia, Beijing, China. E-mail: liulu_mark@163.com; yx_xy1101@126.com.
[3]Rice University, Department of Earth, Environmental and Planetary Sciences, Houston, Texas, USA. E-mail: niu@rice.edu.
[4]BGP Inc., China National Petroleum Corporation, Beijing Research Center, Beijing, China. E-mail: wu.wei@cnpc.com.cn.
[5]SLB, Houston, Texas, USA. E-mail: tanghengyu@gmail.com.
[6]China University of Petroleum-Beijing, College of Geophysics, Beijing, China. E-mail: ljm_cup@sina.com.
[7]Chinese Academy of Science, Institute of Geology and Geophysics, Beijing, China. E-mail: yiyao16@mail.iggcas.ac.cn.

DOI:10.1190/geo2023-0354.1

tropic media, the main theory for P/S wave-mode decomposition is calculating the polarization direction (Dellinger and Etgen, 1990; Tsvankin, 2012). The analytic solution for P/S wave-mode decomposition can be only obtained in the wavenumber domain (Tsvankin, 2012), which is only applicable to homogeneous media.

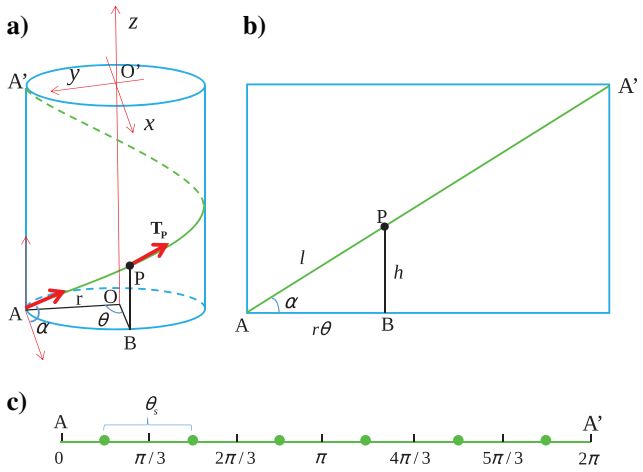

Figure 1. Diagram of the conventional winding configuration of helical fiber. (a) Helical fiber winding along the wellbore, (b) side expanding view of (a), and (c) horizontal view of helical fiber AA' in the rotating angle domain. The cylinder represents the wellbore, green line AA' represents the helical fiber, A is the starting point, and A' is the ending point in one 2π winding period; the green points denote that six sampling points are averagely detected in helical fiber AA' with the angular sampling interval $\theta_s = \pi/3$; P is an arbitrary point in line AA'; B is the projection of point P in the base circle; OO' is the center axis of the cylinder; $\mathbf{T_p}$ indicates the tangent vector of point P; r is the winding radius of the cylinder; θ is the rotating angle; α is the pitch angle; h represents the height $|PB|$ of point P; and l is the length of $|AP|$ and is the coordinate variable in the line AA'. Note that the AA' is measured by length in (a) and (b) and by its rotating angle in (c).

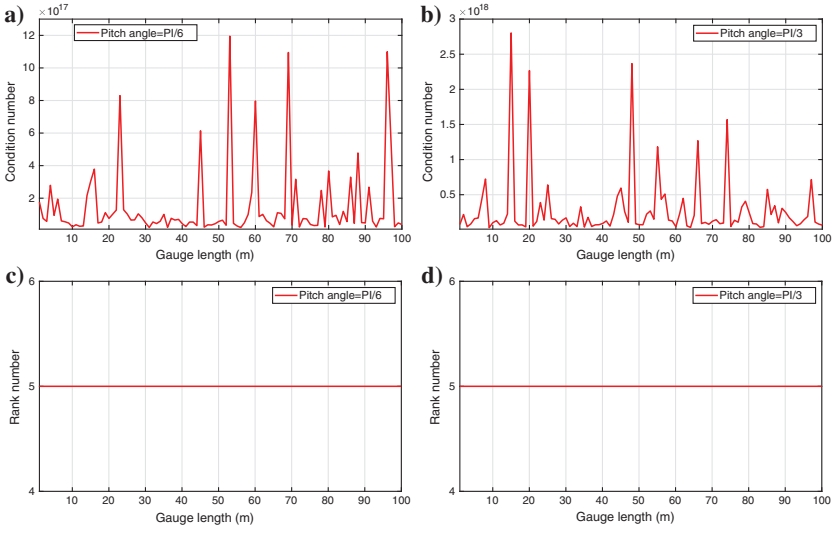

Figure 2. The condition number and rank curves of the projecting matrix for a common winding configuration. (a) Condition number and (c) rank with pitch angle $\alpha = \pi/6$, and (b) condition number and (d) rank with pitch angle $\alpha = \pi/3$. The minimum value of the curves (a and b) are 1.97×10^{16} and 2.98×10^{16}.

To address this problem, the local Fourier transform (Zhang and McMechan, 2010), nonstationary filtering (Yan and Sava, 2009), low-rank approximation (Cheng and Fomel, 2014; Wang et al., 2018), and pseudo-Helmholtz decomposition (Yang et al., 2019; Zuo et al., 2022) are developed to improve the model adaptability. These methods are effective but computationally expensive, especially in 3D cases. Recently, Zhang et al. (2022) propose an efficient space-wavenumber domain decoupled P/S operator for anisotropic ERTM that can produce images with correct amplitudes and phases.

The separated qP- and qS-waves originate from the source and receiver wavefields in ERTM. The quality of the source-side wavefields mainly depends on the initial elastic and anisotropic models (such as P-/S-wave velocity, density, ε, and δ), which can be obtained from full-waveform inversion (e.g., Liu et al., 2015; Ren and Liu, 2015; Chen and Sacchi, 2017) and tomography (e.g., Lo and Inderwiesen, 2012). The receiver wavefields, except for the initial models, are also determined by seismic records that can be detected via geophones or distributed acoustic sensing (DAS) technology. In this paper, we apply the strain field components reconstructed by the DAS response to 3D anisotropic ERTM for receiver wavefield modeling. To improve efficiency, we also extend the space-wavenumber domain P/S decomposition (Zhang et al., 2022) to 3D VTI media, which produces correct P/S wavefields for ERTM images.

As a new acquisition tool, DAS has grown rapidly in theory development and industrial applications (Willis, 2022). Owing to the heterogeneous property of optical fiber, DAS can use a phase signal from a Rayleigh backscattered wave to produce a strain response. Up to the present, DAS technology has been widely used in earthquake monitoring (Lindsey et al., 2020), vertical seismic profile (VSP) reservoir prediction (Mateeva et al., 2014; Zhan and Nahm, 2020), near-surface characterization (Dou et al., 2017), and full-waveform inversion (Egorov et al., 2018; Eaid et al., 2020). Because the optical fiber material is cost friendly, researchers can deploy a long-distance array and obtain highly dense DAS sampling data with a wide frequency band. Moreover, the optical fiber of DAS is more feasible than geophones in downhole environments. All these advantages indicate that DAS technology has potential value in anisotropic ERTM.

However, DAS technology also presents several challenges. The DAS response is sensitive only to the direction along the deployed optic fiber. The seismic records with single straight fiber (such as VSP DAS) can only obtain the single component, which is insufficient for multicomponent imaging in ERTM. To solve this problem, a helical-winding fiber configuration was developed (Ning and Sava, 2018b). The DAS response along the tangential direction of helical fiber can be seen as the projection of original seismic strain components. Therefore, after obtaining the projecting matrix of the helical fiber, the least-squares solution can be built to reconstruct the original seismic strain tensor. Innanen (2017) derives the tangent vector of helix fiber and recovers the P-wave strain tensor with arbitrary and nested-helix winds. Ning and Sava (2018b) describe the concept and theory of multicomponent DAS, which shows that six sampled

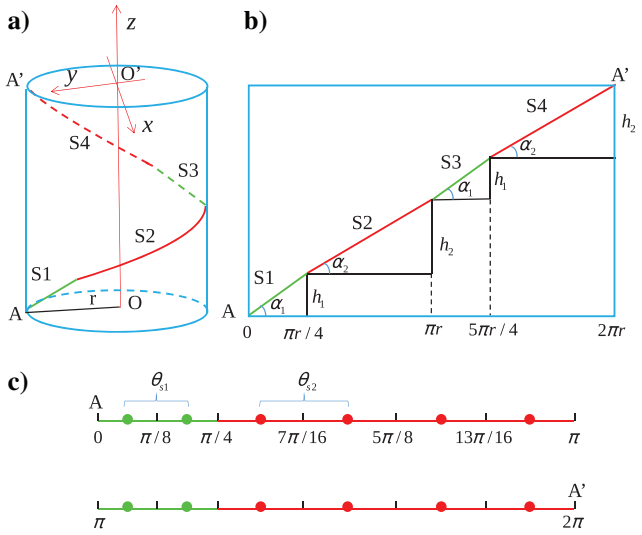

Figure 3. Diagram of the proposed nonregular variant pitch-angle winding configuration of helical fiber. (a) Helical fiber winding along the wellbore, (b) side expanding view of (a), and (c) horizontal view of helical fiber AA' in the rotating angle domain. The cylinder represents the wellbore, and line AA' represents the helical fiber that is split into four segments: S1, S2, S3, and S4. Here, A is the starting point, and A' is the ending point in one 2π winding period. The green points denote that two sampling points are separately detected in the S1 and S3 segments with the angular sampling interval $\theta_{s1} = \pi/3$ and pitch angle α_1, the red points denote that four sampling points are separately detected in the S2 and S4 segments with the angular sampling interval $\theta_{s2} = \pi/6$ and pitch angle α_2, OO' is the center axis of the cylinder, and r is the winding radius of the cylinder. Note that the AA' is measured by its length in (a and b) and by its rotating angle in (c).

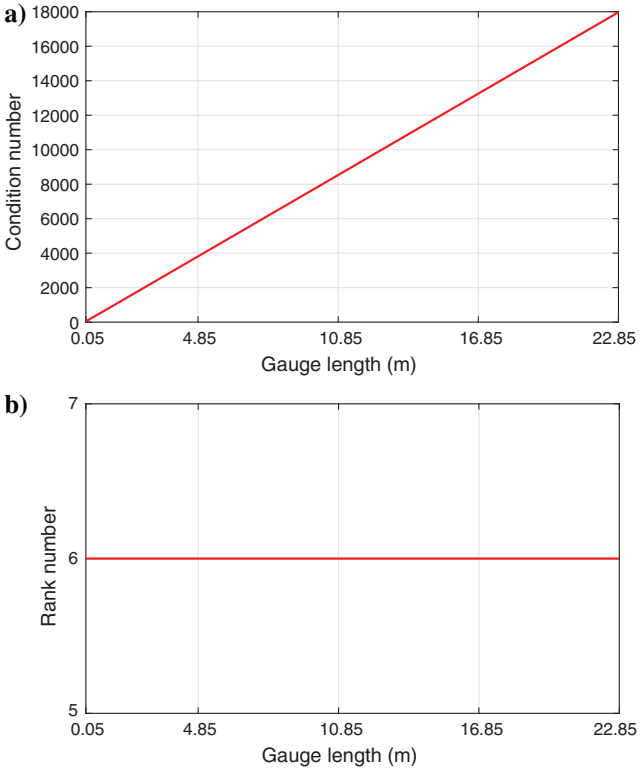

Figure 4. (a) Condition number and (b) rank curves of the projecting matrix for the proposed winding configuration. The minimum value of the curve in (a) is 48.14.

points of the DAS response are required within the seismic wavelength for strain reconstruction. Ning and Sava (2018a) use six optical fibers (five helical fibers and one straight fiber) to acquire different strain projections at the same location. This method avoids the assumption that the seismic wavelength is larger than the six-point sampled window of the DAS response but is difficult to implement in practice. Eaid et al. (2020) combine the geophone and DAS data with shaped fibers to perform the multiple parameter full-waveform inversion. They derive the projecting formulation for the shaped fibers and analyze the scattering radiation patterns of the DAS response. Ning and Sava (2018c) perform the DAS imaging experiment with a scalar energy form condition by using six helical fibers. However, the detailed mathematical derivation and image quality need to be further improved.

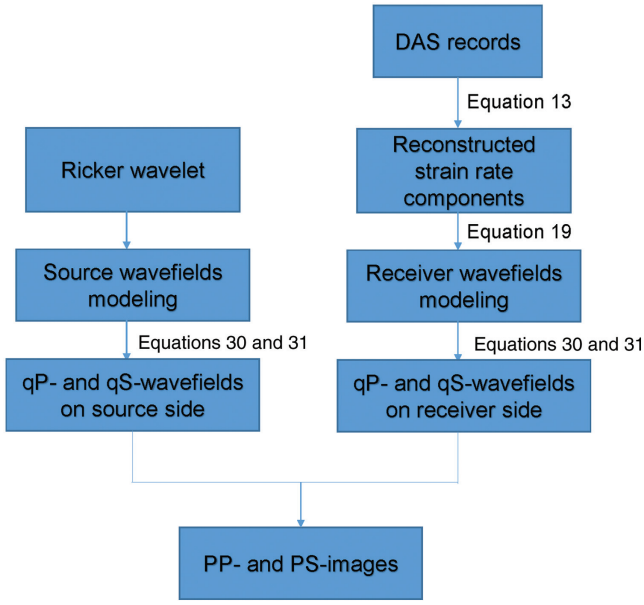

Figure 5. The workflow of 3D VTI DAS-ERTM by using helical fiber DAS records.

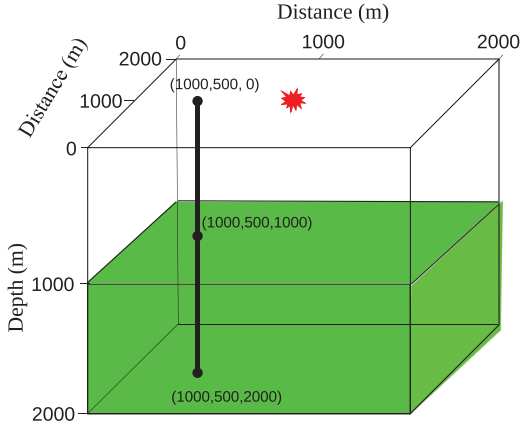

Figure 6. The VTI layered model with vertical wellbore geometry. The red explosion denotes a single shot, the black vertical line represents the wellbore winded by helical fiber, and the reflector is located at a depth of 1000 m.

Although helical-winding fiber DAS technology has been used in seismic imaging and inversion, to date, there is no analytical formulation for original strain tensor reconstruction using helical fiber. In this paper, we build a mathematical relationship among helical fiber parameters. The tangential vector for any point in the helical fiber is derived and used to form the projecting matrix for the DAS response. Furthermore, we propose a variant pitch-angle helix winding configuration that can solve the ill-projecting matrix problem of a regular helical fiber configuration. The least-squares solution is obtained from our configuration for strain vector field reconstruction according to the projection relation. The recovered strain components are backpropagated in ERTM. In summary, we develop an innovative helical fiber winding configuration to recover the strain field components and apply these recovered records to anisotropic ERTM imaging. We also propose a 3D space-wavenumber domain decoupled operator for anisotropic P/S wave decomposition. Both methods help to build a complete DAS-ERTM workflow.

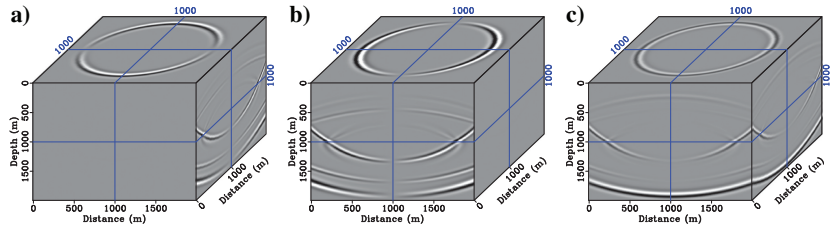

Figure 7. (a) The x-, (b) y-, and (c) z-components of elastic wavefields for the VTI layered model at a propagating time of 0.8 s.

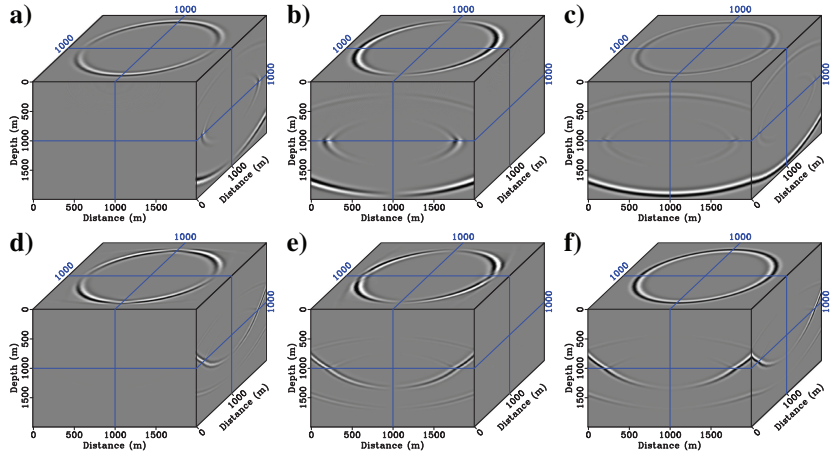

Figure 8. (a) The x-, (b) y-, and (c) z-components of the separated qP-wavefields and (d) x-, (e) y-, and (f) z-components of the separated qS-wavefields for the VTI layered model at a propagating time of 0.8 s.

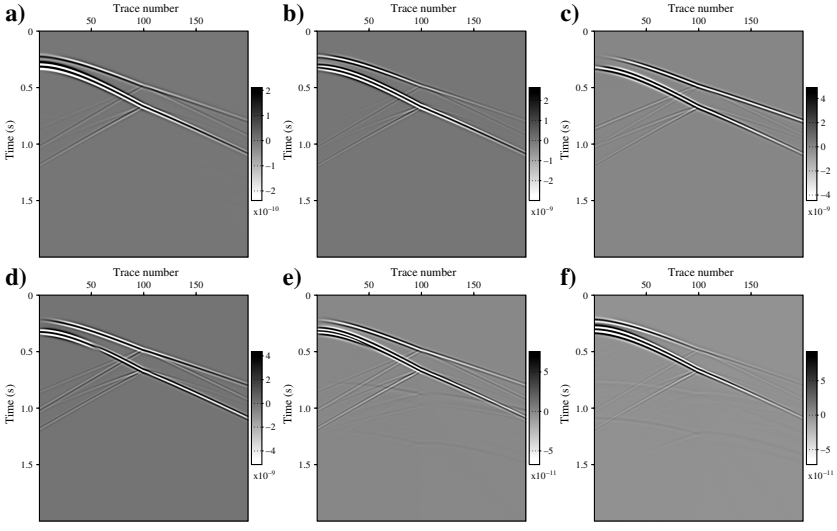

Figure 9. Exact strain rate records (a) $\dot{\varepsilon}_{xx}$, (b) $\dot{\varepsilon}_{yy}$, (c) $\dot{\varepsilon}_{zz}$, (d) $\dot{\varepsilon}_{yz}$, (e) $\dot{\varepsilon}_{xz}$, and (f) $\dot{\varepsilon}_{xy}$ of the VTI layered model with a recording length of 2 s.

METHODOLOGY

In this section, we mainly introduce two innovative algorithms used for the DAS-ERTM workflow. The first algorithm is to use the DAS records to reconstruct the strain rate components by our proposed variant pitch-angle winding configuration. Then, we perform the source and receiver wavefield modeling and obtain the elastic wave snapshot at each time point. The second algorithm is to decompose these 3D VTI elastic waves into vector P and S wavefields with the correct amplitudes and phases. Finally, a dot product elastic imaging condition is applied to produce PP and PS images.

DAS response generated by the helical-winding fiber

This subsection mainly describes the basic mathematical principle of the helical fiber DAS. The DAS response for a point on the helical-winding fiber is the projection of the seismic strain components along the tangential direction of the fiber. It can be expressed as the rotation from the global coordinate system (x, y, z) to the local system (t, m, n) as

$$\varepsilon_0 = \mathbf{M}\varepsilon\mathbf{M}^T, \tag{1}$$

where ε_0 and ε are the rotated and original strain tensors, respectively, and $\mathbf{M}$ is the rotating matrix which can be written as

$$\mathbf{M} = \begin{bmatrix} M_{tx} & M_{ty} & M_{tz} \\ M_{px} & M_{py} & M_{pz} \\ M_{qx} & M_{qy} & M_{qz} \end{bmatrix}, \tag{2}$$

where M_{ij} $(i = t, m, n;\ j = t, p, q)$ is the cosine of the angle between two axes. Because the optic fiber is only sensitive to the tangent direction, we make the t-axis in the local coordinate system parallel to the tangent vector of the helical fiber. In the meantime, it is assumed that the wave-

length is large enough to keep the strain field constant over the gauge length. After that, the DAS response ε_d of the helical-winding fiber can be given by

$$\varepsilon_d = G_{xx}\varepsilon_{xx} + G_{yy}\varepsilon_{yy} + G_{zz}\varepsilon_{zz} + G_{yz}\varepsilon_{yz} + G_{xz}\varepsilon_{xz} + G_{xy}\varepsilon_{xy}, \tag{3}$$

with

$$\begin{aligned}
G_{xx} &= \frac{1}{\mathrm{GL}}\int_{s_p-\mathrm{GL}/2}^{s_p+\mathrm{GL}/2} M_{tx}^2 dl,\\
G_{yy} &= \frac{1}{\mathrm{GL}}\int_{s_p-\mathrm{GL}/2}^{s_p+\mathrm{GL}/2} M_{ty}^2 dl,\\
G_{zz} &= \frac{1}{\mathrm{GL}}\int_{s_p-\mathrm{GL}/2}^{s_p+\mathrm{GL}/2} M_{tz}^2 dl,\\
G_{yz} &= \frac{1}{\mathrm{GL}}\int_{s_p-\mathrm{GL}/2}^{s_p+\mathrm{GL}/2} 2M_{ty}M_{tz} dl,\\
G_{xz} &= \frac{1}{\mathrm{GL}}\int_{s_p-\mathrm{GL}/2}^{s_p+\mathrm{GL}/2} 2M_{tx}M_{tz} dl,\\
G_{xy} &= \frac{1}{\mathrm{GL}}\int_{s_p-\mathrm{GL}/2}^{s_p+\mathrm{GL}/2} 2M_{tx}M_{ty} dl,
\end{aligned} \tag{4}$$

where ε_{xx}, ε_{yy}, and ε_{zz} are normal strain components and ε_{yz}, ε_{xz}, and ε_{xy} are shear strain components. Here, s_p represents the position of the sampling point in the helical fiber, l represents the coordinate variable in the helical fiber, and GL is the gauge length. Equations 3 and 4 indicate that the DAS response is the average of the original strain projection on the GL length.

To obtain M_{tx}, M_{ty}, and M_{tz} of equation 4, we use one 2π winding period of helical fiber configuration and its expanded side view to derive the tangent vector of an arbitrary point in the helical fiber. As shown in Figure 1a, A and A' are the starting and ending points of the optical fiber. Here, r is the winding radius along the wellbore; α and θ are the pitch angle and rotating angle, respectively; P is an arbitrary point in the helical fiber; and $\mathbf{T_p}$ is the tangent vector of point P. In the side view (Figure 1b), we define the height h of point P and the distance AP = l (l is the 1D coordinate variable in line AA'). According to the geometric relationship, we can obtain

$$\cos\alpha = \frac{r\theta}{l}, \quad \sin\alpha = \frac{h}{l}. \tag{5}$$

Equation 5 is an important transformation between helical fiber length l and its corresponding rotation angle θ. The θ range from $[0, 2\pi]$ ($\theta = 0$ at point A and $\theta = 2\pi$ at point A') and maximum $l_{\max} = 2\pi r/\cos\alpha$. In terms of equation 5, the curve equation of helical fiber to the point P can be expressed as

$$\begin{cases} P_x(\theta) = r\sin\theta \\ P_y(\theta) = r\cos\theta, \\ P_z(\theta) = r\theta\tan\alpha \end{cases} \quad \theta \in [0, 2\pi], \tag{6}$$

or

$$\begin{cases} P_x(l) = r\sin(l\cos\alpha/r) \\ P_y(l) = r\cos(l\cos\alpha/r), \\ P_z(l) = l\sin\alpha \end{cases} \quad l \in [0, l_{\max}], \tag{7}$$

where P_x, P_y, and P_z are the coordinates of point P. Equations 6 and 7 indicate both l and θ can be used as the self-variables for the curve function of AA'. However, because equations 6 and 7 mainly

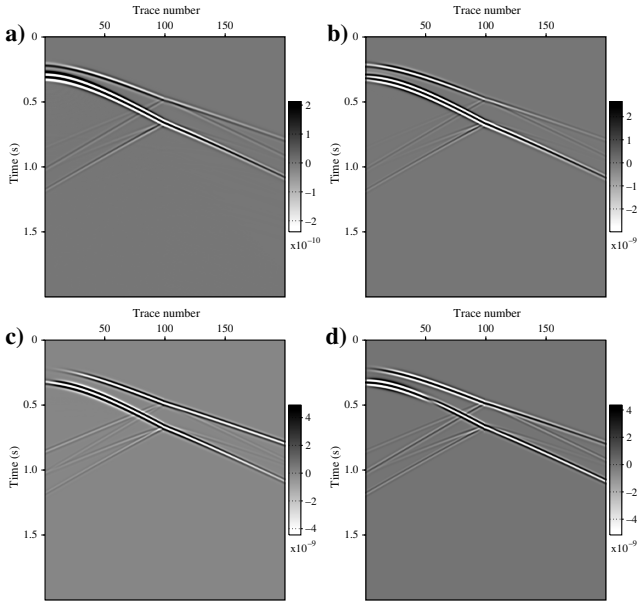

Figure 10. Reconstructed strain rate records (a) $\dot{\varepsilon}_{xx}$, (b) $\dot{\varepsilon}_{yy}$, (c) $\dot{\varepsilon}_{zz}$, (d) $\dot{\varepsilon}_{yz}$, (e) $\dot{\varepsilon}_{xz}$, and (f) $\dot{\varepsilon}_{xy}$ of the VTI layered model via equations 13 and 18 with a gauge length of 1.25 m.

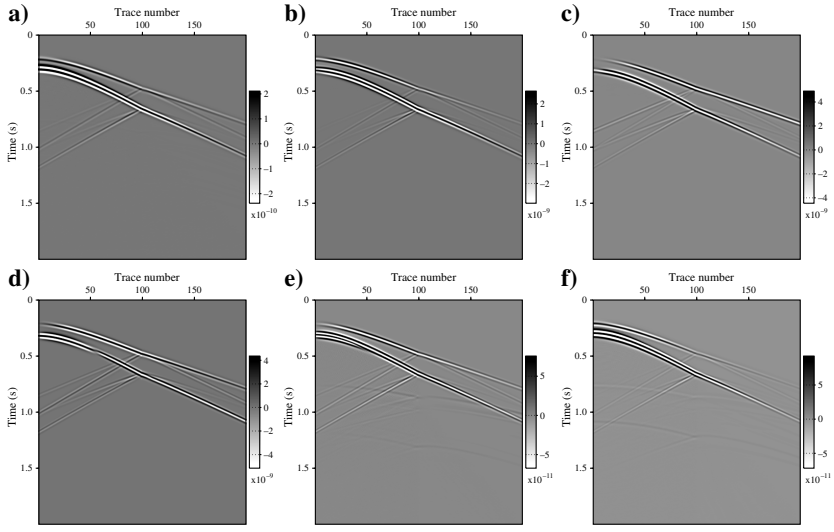

Figure 11. Reconstructed strain rate records (a) $\dot{\varepsilon}_{xx}$, (b) $\dot{\varepsilon}_{yy}$, (c) $\dot{\varepsilon}_{zz}$, (d) $\dot{\varepsilon}_{yz}$, (e) $\dot{\varepsilon}_{xz}$, and (f) $\dot{\varepsilon}_{xy}$ of the VTI layered model via equations 13 and 18 with a gauge length of 4.85 m.

contain trigonometric functions, we prefer using θ to describe curve AA'. Thus, the unit tangent vector $\mathbf{T_p}$ can be expressed as

$$\mathbf{T_p} = \frac{\left(\frac{dP_x(\theta)}{d\theta}, \frac{dP_y(\theta)}{d\theta}, \frac{dP_z(\theta)}{d\theta}\right)}{\sqrt{\left(\frac{dP_x(\theta)}{d\theta}\right)^2 + \left(\frac{dP_y(\theta)}{d\theta}\right)^2 + \left(\frac{dP_z(\theta)}{d\theta}\right)^2}} = (\cos\,\alpha\,\cos\,\theta, -\cos\,\alpha\,\sin\,\theta, \sin\,\alpha)^T. \quad (8)$$

Equation 8 is also presented in Innanen (2017) and Eaid et al. (2020) with other alternative parameters. By setting the base vector $\mathbf{x} = (1, 0, 0)$, $\mathbf{y} = (0, 1, 0)$, and $\mathbf{z} = (0, 0, 1)$ in the global coordinate system, we can calculate the projecting coefficient M_{tx}, M_{ty}, and M_{tz} as

$$\begin{aligned} M_{tx} &= \mathbf{T_p} \cdot \mathbf{x} = \cos\,\alpha\,\cos\,\theta, \\ M_{ty} &= \mathbf{T_p} \cdot \mathbf{y} = -\cos\,\alpha\,\sin\,\theta, \\ M_{tz} &= \mathbf{T_p} \cdot \mathbf{z} = \sin\,\alpha. \end{aligned} \quad (9)$$

Then, we substitute equation 9 into equation 4 and replace the l with θ to obtain

$$\begin{aligned} G_{xx} &= A_0 \int_{\theta_p-\theta_g}^{\theta_p+\theta_g} \cos^2\,\alpha \cos^2\,\theta d\theta, \\ G_{yy} &= A_0 \int_{\theta_p-\theta_g}^{\theta_p+\theta_g} \cos^2\,\alpha \sin^2\,\theta d\theta, \\ G_{zz} &= A_0 \int_{\theta_p-\theta_g}^{\theta_p+\theta_g} \sin^2\,\alpha d\theta, \\ G^i_{yz} &= A_0 \int_{\theta_p-\theta_g}^{\theta_p+\theta_g} -2\,\sin\,\alpha\,\cos\,\alpha\,\sin\,\theta d\theta, \\ G^i_{xz} &= A_0 \int_{\theta_p-\theta_g}^{\theta_p+\theta_g} 2\,\sin\,\alpha\,\cos\,\alpha\,\cos\,\theta d\theta, \\ G^i_{xy} &= A_0 \int_{\theta_p-\theta_g}^{\theta_p+\theta_g} -2\cos^2\,\alpha\,\sin\,\theta\,\cos\,\theta d\theta, \end{aligned} \quad (10)$$

where $\theta_p = s_p\,\cos\,\alpha/r$ is the angular position of the sampling point. The term $\theta_g = \mathrm{GL}/2 \cdot \cos\,\alpha/r$ represents the angle related to the gauge length and $A_0 = r/(\mathrm{GL} \cdot \cos\,\alpha)$ is the weighted coefficient. The DAS response of a single point in the helical fiber can be obtained by substituting equation 10 with equation 3.

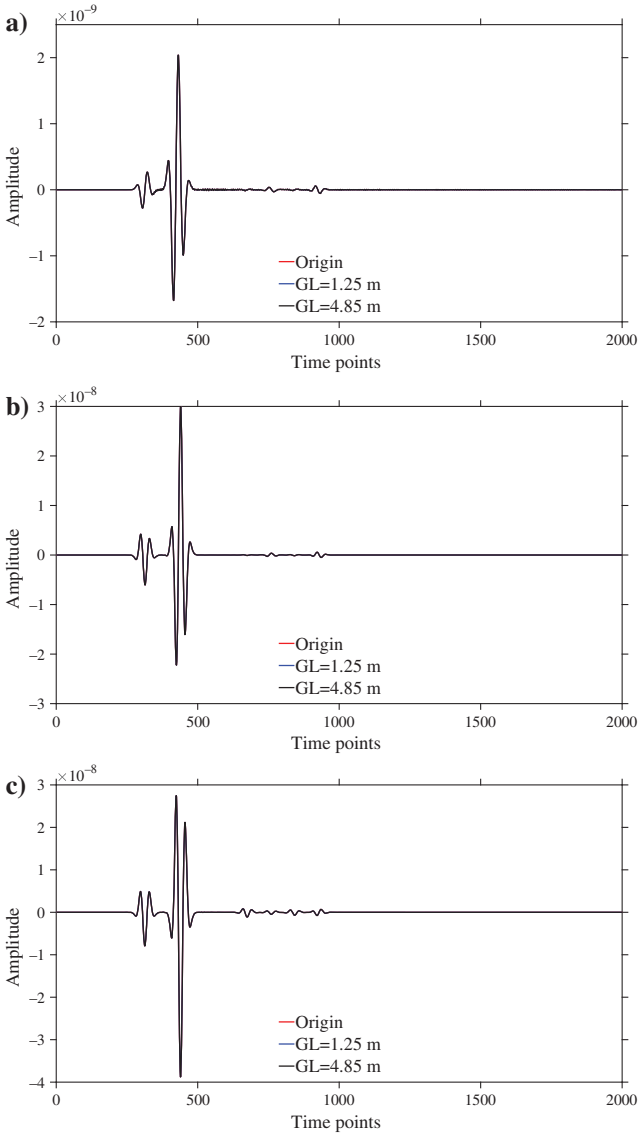

Figure 12. Comparison of single trace data (a) $\dot{\varepsilon}_{xx}$, (b) $\dot{\varepsilon}_{yy}$, (c) $\dot{\varepsilon}_{zz}$, (d) $\dot{\varepsilon}_{yz}$, (e) $\dot{\varepsilon}_{xz}$, and (f) $\dot{\varepsilon}_{xy}$ extracted from the original (Figure 9) and DAS reconstructed strain rate records (Figures 10 and 11). The red line denotes the original exact trace data, the blue line represents the reconstructed data with a gauge length of 1.25 m, and the black line indicates the reconstructed data with a gauge length of 4.85 m.

Variant pitch-angle winding configuration for helical fiber

Equations 3 and 10 indicate a single point of the DAS response from the helical fiber. However, at least six values of ε_d are required to reconstruct the original strain field components $\varepsilon_{xx}, \varepsilon_{yy}, \varepsilon_{zz}, \varepsilon_{yz}, \varepsilon_{xz}, \varepsilon_{xy}$ in equation 3. For the common winding configuration (Figure 1), we can averagely split the helical fiber into six segments and detect the seismic signal at the midpoint of every segment, which is shown in Figure 1c. For simplicity, we are supposed to sample six points of the DAS response in one 2π period (we will extend it to an arbitrary number of winding periods subsequently for six-point sampling). The projecting matrix coefficients for the configuration of Figure 1 are written as

$$G^i_{xx} = A_0 \int_{\theta_b+(i-1)\theta_s-\theta_g}^{\theta_b+(i-1)\theta_s+\theta_g} \cos^2\alpha\cos^2\theta d\theta,$$

$$G^i_{yy} = A_0 \int_{\theta_b+(i-1)\theta_s-\theta_g}^{\theta_b+(i-1)\theta_s+\theta_g} \cos^2\alpha\sin^2\theta d\theta,$$

$$G^i_{zz} = A_0 \int_{\theta_b+(i-1)\theta_s-\theta_g}^{\theta_b+(i-1)\theta_s+\theta_g} \sin^2\alpha d\theta,$$

$$G^i_{yz} = A_0 \int_{\theta_b+(i-1)\theta_s-\theta_g}^{\theta_b+(i-1)\theta_s+\theta_g} -2\sin\alpha\cos\alpha\sin\theta d\theta,$$

$$G^i_{xz} = A_0 \int_{\theta_b+(i-1)\theta_s-\theta_g}^{\theta_b+(i-1)\theta_s+\theta_g} 2\sin\alpha\cos\alpha\cos\theta d\theta,$$

$$G^i_{xy} = A_0 \int_{\theta_b+(i-1)\theta_s-\theta_g}^{\theta_b+(i-1)\theta_s+\theta_g} -2\cos^2\alpha\sin\theta\cos\theta d\theta, \qquad (11)$$

where $i \in [1,6]$ represents the serial number of the six sampling points (from left to right in Figure 1c), θ_s is the sampling angular interval and is equal to $\pi/3$ in the winding configuration. The spatial sampling interval is $s = r\theta_s/\cos\alpha + 2N\pi r/\cos\alpha$. Here, N is a nonnegative integer and $N = 0$ means that six sampling points are extracted in one 2π winding period (Figure 1c). The term $\theta_b = \theta_s/2$ is the angular position of the beginning sampling point. Substituting equation 11 into equation 3, we obtain the vector form of the DAS response as

$$\boldsymbol{\varepsilon}_d = \mathbf{G}\boldsymbol{\varepsilon}, \qquad (12)$$

where $\boldsymbol{\varepsilon} = [\varepsilon_{xx}\ \varepsilon_{yy}\ \varepsilon_{zz}\ \varepsilon_{yz}\ \varepsilon_{xz}\ \varepsilon_{xy}]^T$ is the strain vector that we aim to construct, and $\boldsymbol{\varepsilon}_d$ is a column vector containing six different DAS response values. Here, $\mathbf{G}$ is a 6×6 matrix with the same formation $(G^i_{xx}\ G^i_{yy}\ G^i_{zz}\ G^i_{yz}\ G^i_{xz}\ G^i_{xy})$ in each i row. Having once obtained the DAS records of the six points within the seismic wavelength, it is convenient to form the least-squares solution for the original strain components as

$$\boldsymbol{\varepsilon} = (\mathbf{G}^T\mathbf{G})^{-1}\mathbf{G}^T\boldsymbol{\varepsilon}_\mathbf{d}. \qquad (13)$$

Equation 13 is used for original strain component reconstruction for 3D VTI elastic ERTM. The quality of the reconstructed $\boldsymbol{\varepsilon}$ depends on the projecting matrix $\mathbf{G}$, which can be validated by its rank and condition number. According to equation 11, the matrix $\mathbf{G}$ is determined by the angular sampling interval θ_s, pitch angle α, and gauge length GL. The term $\theta_s = \pi/3$ remains constant, and for pitch angles α, we give two test values, 30° and 60°. The gauge length ranges from 0.1 to 10 m. Substituting these parameters into equation 11, we calculate the condition number and rank curves (Figure 2) of the projecting matrix $\mathbf{G}$. Surprisingly, Figure 2 exhibits very high values of the condition number with the preceding parameters, even if the minimum value is beyond 10^{16}. Its rank number is five, which indicates that the projecting matrix is singular. Therefore, it is difficult to calculate the inverse of the matrix $\mathbf{G}$ to reconstruct the seismic strain components by using a regular winding configuration (Figure 1).

To solve the ill-conditioned matrix problem in the conventional winding method, we propose a nonregular variant pitch-angle configuration (Figure 3) for helical fiber. In our proposed configuration, 12 points are exactly taken at a fixed position from one or several winding periods of 2π with constant spatial sampling interval s. For simplicity, we plot the design with one 2π winding period in Figure 3.

As observed, the helical fiber (Figure 3a) is split into four segments. Specifically, in the first (S1) and third (S3) segments (the green lines in Figure 3), two sampling points are detected at the mid of the line segment (Figure 3c) with the pitch angle α_1 (Figure 3b) and angular sampling interval $\theta_{s1} = \pi/8$ (Figure 3c). In the second (S2) and fourth (S4) segmentation (the red lines in

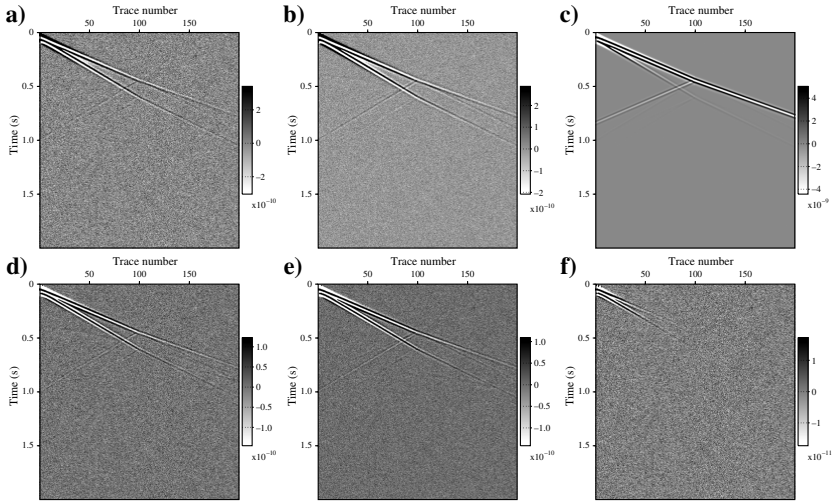

Figure 13. Reconstructed strain rate records (a) $\dot{\varepsilon}_{xx}$, (b) $\dot{\varepsilon}_{yy}$, (c) $\dot{\varepsilon}_{zz}$, (d) $\dot{\varepsilon}_{yz}$, (e) $\dot{\varepsilon}_{xz}$, and (f) $\dot{\varepsilon}_{xy}$ of the VTI layered model with the random noise of the DAS data amplitude in its frequency band.

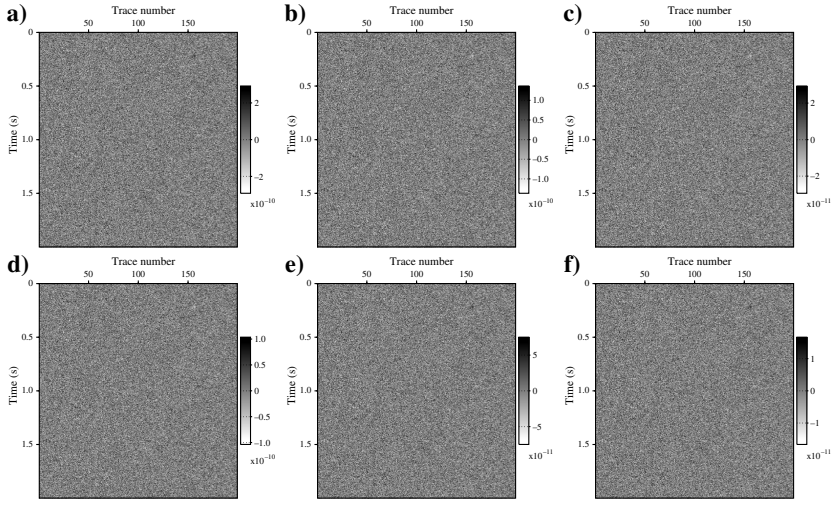

Figure 14. Random noise extracted from the difference between the reconstructed and original strain rate records (a) $\dot{\varepsilon}_{xx}$, (b) $\dot{\varepsilon}_{yy}$, (c) $\dot{\varepsilon}_{zz}$, (d) $\dot{\varepsilon}_{yz}$, (e) $\dot{\varepsilon}_{xz}$, and (f) $\dot{\varepsilon}_{xy}$ of the VTI layered model.

Figure 3), four points are acquired at the center of the line segment with the pitch angle α_2 (Figure 3b) and angular sampling interval $\theta_{s2} = 3\pi/16$ (Figure 3c). The six sampling points in S1 and S2 segments $[0, \pi]$ and S3 and S4 segments $[\pi, 2\pi]$ are used to reconstruct different strain fields, respectively. As one can see in the side view (Figure 3b), these helical fiber parameters fulfill the trigonometric relationship in equation 5. Therefore, we can derive the curve equation of the four segments with an arbitrary point P on the helical fiber of Figure 3a as

$$\begin{cases} P_x(\theta) = r\sin\theta,\ \theta\in[0,2\pi] \\ P_y(\theta) = r\cos\theta,\ \theta\in[0,2\pi] \\ P_z(\theta) = r\theta\tan\alpha_1,\ \theta\in[0,\pi/4]_{S1} \\ P_z(\theta) = \frac{\pi}{4}r\tan\alpha_1 + (\theta-\pi/4)r\tan\alpha_2,\ \theta\in[\pi/4,\pi]_{S2} \\ P_z(\theta) = \frac{\pi}{4}r\tan\alpha_1 + \frac{3\pi}{4}r\tan\alpha_2 + (\theta-\pi)r\tan\alpha_1,\ \theta\in[\pi,5\pi/4]_{S3} \\ P_z(\theta) = \frac{\pi}{2}r\tan\alpha_1 + \frac{3\pi}{4}r\tan\alpha_2 + (\theta-5\pi/4)r\tan\alpha_2,\ \theta\in[5\pi/4,2\pi]_{S4} \end{cases}. \tag{14}$$

In terms of equation 14, four segments share identical P_x and P_y expressions but different P_z coordinates. Substituting equation 14 into equation 8, we can obtain the same form of tangent vector $\mathbf{T_p}$ in equation 8 but with two pitch angles α_1 and α_2. Concurrently, the sampling interval s and gauge length GL are required to be constant in the entire seismic signal acquisition processing and are designed according to the transformation relationship of equation 5 as

$$\begin{aligned} s &= \frac{r\theta_{s1}}{\cos\alpha_1} + Nr\left(\frac{\pi}{2\cos\alpha_1} + \frac{3\pi}{2\cos\alpha_2}\right) \\ &= \frac{r\theta_{s2}}{\cos\alpha_2} + Nr\left(\frac{\pi}{2\cos\alpha_1} + \frac{3\pi}{2\cos\alpha_2}\right), \\ \mathrm{GL}/2 &= \frac{r\theta_{s1}/2}{\cos\alpha_1} + Mr\left(\frac{\pi}{2\cos\alpha_1} + \frac{3\pi}{2\cos\alpha_2}\right) \\ &= \frac{r\theta_{s2}/2}{\cos\alpha_2} + Mr\left(\frac{\pi}{2\cos\alpha_1} + \frac{3\pi}{2\cos\alpha_2}\right), \end{aligned} \tag{15}$$

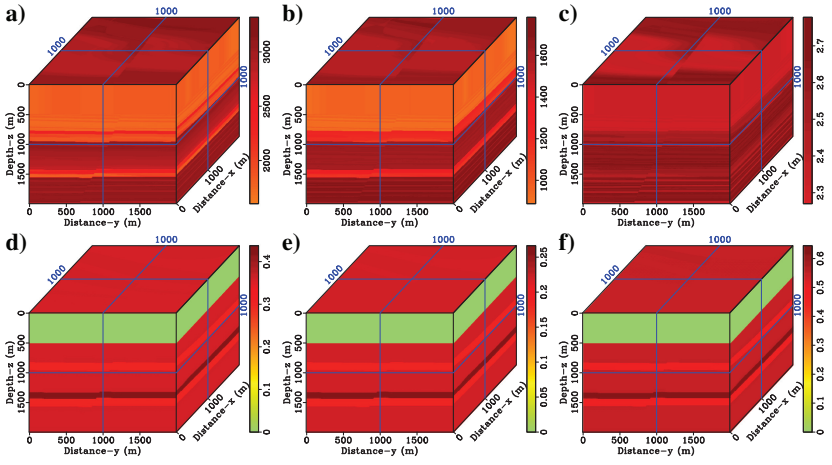

Figure 15. (a) The P-wave velocity, (b) S-wave velocity, (c) density, (d) ϵ, (e) δ, and (f) γ for the 3D VTI arid model.

where N is a nonnegative integer and indicates the number of 2π winding periods between two sampling points. The value of N will not influence the integration of equations 11 and 16 due to the fact that the tangent vector formation (equation 8) is identical at the same position of the different winding periods. In addition, α_1 and α_2 are required to fulfill the relationship $\cos\alpha_1/\cos\alpha_2 = 2/3$ according to equation 15. Here, M is also a nonnegative integer and determines the gauge length. The reason we set such formation of GL in equation 15 is that a gauge length-related angle can be expressed as $\theta_g = \theta_{s1}/2 + 2M\pi$ or $\theta_{s2}/2 + 2M\pi$, which is convenient for the integration of equation 16. Because the formation of a tangent vector is identical in our proposed (Figure 3) and conventional configurations (Figure 1), we directly substitute those preceding parameters into equation 11. Taking the S1 and S2 segments as an example, we can obtain the coefficients of the projecting matrix $\mathbf{G}$ for our proposed winding design as

$$\begin{aligned} G^i_{xx} &= A_0\int_{\theta^i_b+(i-1)\theta^i_s-\theta^i_g}^{\theta^i_b+(i-1)\theta^i_s+\theta^i_g}\cos^2\alpha\cos^2\theta d\theta, \\ G^i_{yy} &= A_0\int_{\theta^i_b+(i-1)\theta^i_s-\theta^i_g}^{\theta^i_b+(i-1)\theta^i_s+\theta^i_g}\cos^2\alpha\sin^2\theta d\theta, \\ G^i_{zz} &= A_0\int_{\theta^i_b+(i-1)\theta^i_s-\theta^i_g}^{\theta^i_b+(i-1)\theta^i_s+\theta^i_g}\sin^2\alpha d\theta, \\ G^i_{yz} &= A_0\int_{\theta^i_b+(i-1)\theta^i_s-\theta^i_g}^{\theta^i_b+(i-1)\theta^i_s+\theta^i_g}-2\sin\alpha\cos\alpha\sin\theta d\theta, \\ G^i_{xz} &= A_0\int_{\theta^i_b+(i-1)\theta^i_s-\theta^i_g}^{\theta^i_b+(i-1)\theta^i_s+\theta^i_g}2\sin\alpha\cos\alpha\cos\theta d\theta, \\ G^i_{xy} &= A_0\int_{\theta^i_b+(i-1)\theta^i_s-\theta^i_g}^{\theta^i_b+(i-1)\theta^i_s+\theta^i_g}-2\cos^2\alpha\sin\theta\cos\theta d\theta, \end{aligned} \tag{16}$$

with

$$\begin{aligned} \theta^i_b &= \begin{cases} \pi/16, & i=1,2 \\ -\pi/32, & i=3,4,5,6 \end{cases}, \\ \theta^i_s &= \begin{cases} \theta_{s1}=\pi/8, & i=1,2 \\ \theta_{s2}=3\pi/16, & i=3,4,5,6 \end{cases}, \\ \theta^i_g &= \begin{cases} \theta_{s1}/2+2M\pi, & i=1,2 \\ \theta_{s2}/2+2M\pi, & i=3,4,5,6 \end{cases}, \\ \alpha &= \begin{cases} \alpha_1, & i=1,2 \\ \alpha_2, & i=3,4,5,6 \end{cases}, \\ A_0 &= \begin{cases} r/(\mathrm{GL}*\cos\alpha_1), & i=1,2 \\ r/(\mathrm{GL}*\cos\alpha_2), & i=3,4,5,6 \end{cases}, \end{aligned} \tag{17}$$

where i is the serial number of sampling points in the S1 and S2 segments. For calculating the projecting matrix of S3 and S4, we only need to add π to θ^i_b in equation 17. For simplicity, equation 16 can be rewritten as

DOI:10.1190/geo2023-0354.1

$$
\begin{aligned}
G^i_{xx} &= A_0 \int_{\theta^i_b+(i-1)\theta^i_s-(\theta^i_g-2M\pi)}^{\theta^i_b+(i-1)\theta^i_s+(\theta^i_g-2M\pi)} \cos^2\alpha\cos^2\theta d\theta \\
&+ \frac{4Mr}{\mathrm{GL}}\left(\left(\frac{\pi}{8}+\frac{1}{4}\right)\cos\alpha_1+\left(\frac{3\pi}{8}-\frac{1}{4}\right)\cos\alpha_2\right), \\
G^i_{yy} &= A_0 \int_{\theta^i_b+(i-1)\theta^i_s-(\theta^i_g-2M\pi)}^{\theta^i_b+(i-1)\theta^i_s+(\theta^i_g-2M\pi)} \cos^2\alpha\sin^2\theta d\theta \\
&+ \frac{4Mr}{\mathrm{GL}}\left(\left(\frac{\pi}{8}-\frac{1}{4}\right)\cos\alpha_1+\left(\frac{3\pi}{8}+\frac{1}{4}\right)\cos\alpha_2\right), \\
G^i_{zz} &= A_0 \int_{\theta^i_b+(i-1)\theta^i_s-(\theta^i_g-2M\pi)}^{\theta^i_b+(i-1)\theta^i_s+(\theta^i_g-2M\pi)} \sin^2\alpha d\theta \\
&+ \frac{4Mr}{\mathrm{GL}}\left(\frac{\pi}{4}\sin\alpha_1\tan\alpha_1+\frac{3\pi}{4}\sin\alpha_2\tan\alpha_2\right), \\
G^i_{yz} &= A_0 \int_{\theta^i_b+(i-1)\theta^i_s-(\theta^i_g-2M\pi)}^{\theta^i_b+(i-1)\theta^i_s+(\theta^i_g-2M\pi)} -2\sin\alpha\cos\alpha\sin\theta d\theta, \\
G^i_{xz} &= A_0 \int_{\theta^i_b+(i-1)\theta^i_s-(\theta^i_g-2M\pi)}^{\theta^i_b+(i-1)\theta^i_s+(\theta^i_g-2M\pi)} 2\sin\alpha\cos\alpha\cos\theta d\theta, \\
G^i_{xy} &= A_0 \int_{\theta^i_b+(i-1)\theta^i_s-(\theta^i_g-2M\pi)}^{\theta^i_b+(i-1)\theta^i_s+(\theta^i_g-2M\pi)} -2\cos^2\alpha\sin\theta\cos\theta d\theta \\
&+ \frac{4Mr}{\mathrm{GL}}\left(-\frac{1}{2}\cos\alpha_1+\frac{1}{2}\cos\alpha_2\right). \qquad (18)
\end{aligned}
$$

Equation 18 is more friendly for programming than equation 16 because the integral range is limited to one line segment, which only contains one pitch angle for each sampling point. The formation of the projecting matrix for S2 and S4 segments is the same as S1 and S2 and thus does not repeat in this paper. The original strain components are obtained by substituting equation 18 with equation 13.

To test the rank and condition number of the projecting matrix (equation 18) from our proposed variant pitch-angle helical fiber design, we adopt the parameters $r = 0.05$ m, $\alpha_1 = 66.88°$, $\alpha_2 = 53.91°$, $N = 1$, $s = 0.7$ m (the minimum sampling interval in the DAS input/output (IO) instrument FEBUS is 0.2 m); M ranges from 0 to 20; and the gauge length GL is calculated from equation 15 and ranges from 0.05 to 24.05 m. Figure 4 exhibits the condition number of the projecting matrix (equation 18) variation with the GL. As shown, the condition number increases as the gauge length grows. This is caused by the average effects of the gauge length. However, its maximum value is limited to 10^4 orders, which is significantly less than 10^{16} of the conventional configuration (Figure 2), and its minimum value is only 48.14. Concurrently, its rank number remains at six implying a full-rank projecting matrix. Thus, our proposed helical fiber winding design enables an effective reconstruction of the original strain components.

In Figures 1 and 3, we use vertical wellbore to derive the projecting matrix of helical fiber, which is similar to VSP geometry. When applying the surface geometry burying helical fiber in the ground, it is straightforward by exchanging x and z of the projecting matrix in equations 11 and 16. For instance, for surface exploration with helical fiber, G^i_{xx} becomes G^i_{zz}, G^i_{xy} changes to G^i_{yz}, and vice versa.

After reconstructing the strain field with helical fiber, we feed those components to the 3D VTI ERTM. In this paper, we use the first-order stress-velocity elastic wave equation, the convolutional perfectly matched layer boundary condition, and the high-order staggered-grid finite difference to extrapolate anisotropic elastic wavefields. Suppose the DAS IU instrument records the strain rate, which is the temporal derivative of the strain and is also in accord with the analysis in the previous section. The DAS strain rate records can reconstruct the original strain rate field that is then substituted into the first-order stress-velocity elastic wave equation according to

$$
\begin{aligned}
&\dot{\varepsilon}_{xx} = \frac{\partial v_x}{\partial x}, \quad \dot{\varepsilon}_{yy} = \frac{\partial v_y}{\partial y}, \quad \dot{\varepsilon}_{zz} = \frac{\partial v_z}{\partial z}, \quad \dot{\varepsilon}_{yz} = \frac{\partial v_y}{\partial z}+\frac{\partial v_z}{\partial y}, \\
&\dot{\varepsilon}_{xz} = \frac{\partial v_x}{\partial z}+\frac{\partial v_z}{\partial x}, \quad \dot{\varepsilon}_{xy} = \frac{\partial v_y}{\partial x}+\frac{\partial v_x}{\partial y}, \qquad (19)
\end{aligned}
$$

where v_x, v_y, and v_z are the particle velocity in x-, y-, and z-directions. Here, $\dot{\varepsilon}$ denotes the temporal derivative of the strain.

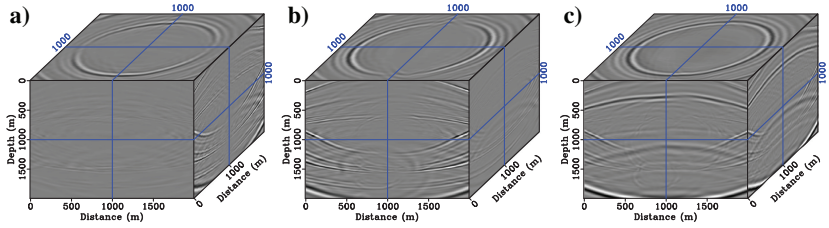

Figure 16. (a) The x-, (b) y-, and (c) z-components of the elastic wavefields for the VTI arid model at a propagating time of 1.0 s.

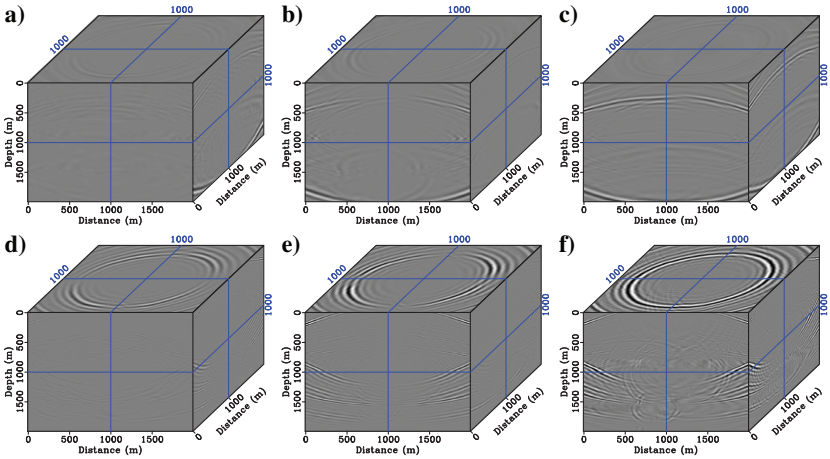

Figure 17. (a) The x-, (b) y-, and (c) z-components of the separated qP-wavefields and (d) x-, (e) y-, and (f) z-components of the separated qS-wavefields for the VTI layered model at a propagating time of 1.0 s.

3D efficient decoupled operator for VTI media

By using equation 19, we extrapolate the receiver wavefields and also calculate the source wavefields. To produce the correct PP and PS images, these elastic wavefields require being separated into P and S wave modes, respectively. This section mainly introduces an efficient decoupled operator in 3D VTI media.

By solving the 3D VTI Christoffel equation with elliptical approximation (Tsvankin, 2012; Zuo et al., 2022), we obtain three eigenvectors as

$$\mathbf{D^P}=\begin{bmatrix}k_x\\k_y\\ak_z\end{bmatrix},\quad \mathbf{D^{SV}}=\begin{bmatrix}-ak_xk_z\\-ak_yk_z\\k_x^2+k_y^2\end{bmatrix},\quad \mathbf{D^{SH}}=\begin{bmatrix}k_y\\-k_x\\0\end{bmatrix},\tag{20}$$

with

$$a=\frac{\sqrt{[(1+2\delta)v_p^2-v_s^2][v_p^2-v_s^2]}}{(1+2\epsilon)v_p^2-v_s^2},\tag{21}$$

where $\mathbf{D^P},\mathbf{D^{SV}},\mathbf{D^{SH}}$ represent the polarizations of qP-, qSV-, and qSH-waves, respectively. Here, k_x, k_y, and k_z are the wavenumber components in the x-, y-, and z-directions. The terms V_P and V_S are the vertical P- and S-wave velocities, and ϵ and δ are the anisotropic parameters. When $\epsilon=0$ and $\delta=0$, equation 20 can be simplified to an isotropic situation.

The elastic wavefields are composed of qP-, qSV-, and qSH-wave components, which can be expressed as

$$\mathbf{U}=\mathbf{U^P}+\mathbf{U^{SV}}+\mathbf{U^{SH}},\tag{22}$$

where $\mathbf{U}=(U_x,U_y,U_z)$, $\mathbf{U^P}=(U_x^P,U_y^P,U_z^P)$, $\mathbf{U^{SV}}=(U_x^{SV},U_y^{SV},U_z^{SV})$, and $\mathbf{U^{SH}}=(U_x^{SH},U_y^{SH},U_z^{SH})$ are vector elastic, qP-, qSV-, and qSH-wavefields in the wavenumber domain. Based on the Helmholtz decomposition theory, we project the P/S wavefields of equation 22 to three polarization vectors (equation 20) and obtain

$$\begin{aligned}&\mathbf{D^P}\cdot\mathbf{U}=\mathbf{D^P}\cdot\mathbf{U^P},\quad \mathbf{D^{SV}}\cdot\mathbf{U}=\mathbf{D^{SV}}\cdot\mathbf{U^{SV}},\\&\mathbf{D^{SH}}\cdot\mathbf{U}=\mathbf{D^{SH}}\cdot\mathbf{U^{SH}},\quad \mathbf{D^P}\cdot\mathbf{U^{SV}}=0,\\&\mathbf{D^P}\cdot\mathbf{U^{SH}}=0,\quad \mathbf{D^{SV}}\cdot\mathbf{U^P}=0,\quad \mathbf{D^{SV}}\cdot\mathbf{U^{SH}}=0,\\&\mathbf{D^{SH}}\cdot\mathbf{U^P}=0,\quad \mathbf{D^{SH}}\cdot\mathbf{U^{SV}}=0.\end{aligned}\tag{23}$$

Equation 23 includes nine unknown variables and can be easily solved as

$$\begin{aligned}U_x^P&=\frac{k_x(k_xU_x+k_yU_y+ak_zU_z)}{k_x^2+k_y^2+a^2k_z^2},\\U_y^P&=\frac{k_y(k_xU_x+k_yU_y+ak_zU_z)}{k_x^2+k_y^2+a^2k_z^2},\\U_z^P&=\frac{ak_z(k_xU_x+k_yU_y+ak_zU_z)}{k_x^2+k_y^2+a^2k_z^2},\end{aligned}\tag{24}$$

$$\begin{aligned}U_x^{SV}&=\frac{-ak_xk_z(-ak_xk_zU_x-ak_yk_zU_y+k_x^2U_z+k_y^2U_z)}{(k_x^2+k_x^2)(k_x^2+k_y^2+a^2k_z^2)},\\U_y^{SV}&=\frac{-ak_yk_z(-ak_xk_zU_x-ak_yk_zU_y+k_x^2U_z+k_y^2U_z)}{(k_x^2+k_x^2)(k_x^2+k_y^2+a^2k_z^2)},\\U_z^{SV}&=\frac{-ak_xk_zU_x-ak_yk_zU_y+k_x^2U_z+k_y^2U_z}{k_x^2+k_y^2+a^2k_z^2},\end{aligned}\tag{25}$$

and

$$\begin{aligned}U_x^{SH}&=\frac{k_y(k_yU_x-k_xU_y)}{k_x^2+k_y^2},\\U_y^{SH}&=\frac{-k_x(k_yU_x-k_xU_y)}{k_x^2+k_y^2},\quad U_z^{SH}=0.\end{aligned}\tag{26}$$

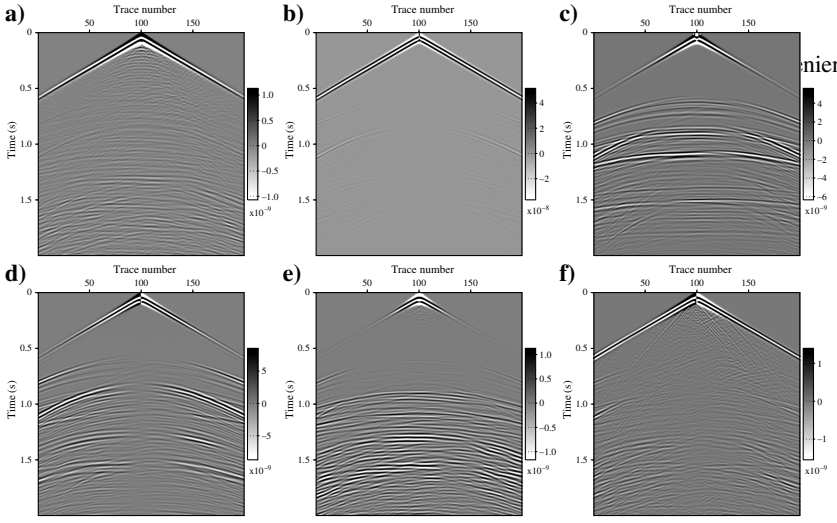

Figure 18. Exact strain rate records (a) $\dot{\varepsilon}_{xx}$, (b) $\dot{\varepsilon}_{yy}$, (c) $\dot{\varepsilon}_{zz}$, (d) $\dot{\varepsilon}_{yz}$, (e) $\dot{\varepsilon}_{xz}$, and (f) $\dot{\varepsilon}_{xy}$ of the VTI arid model with a recording length of 2 s.

nience, the vector form of equations 24–26 can be shown as

$$\begin{aligned}\mathbf{U^P}&=\mathbf{D^P}\left(\mathbf{D^P}\cdot\frac{\mathbf{U}}{|\mathbf{D^P}|^2}\right),\\\mathbf{U^{SV}}&=\mathbf{D^{SV}}\left(\mathbf{D^{SV}}\cdot\frac{\mathbf{U}}{|\mathbf{D^{SV}}|^2}\right),\\\mathbf{U^{SH}}&=\mathbf{D^{SH}}\left(\mathbf{D^{SH}}\cdot\frac{\mathbf{U}}{|\mathbf{D^{SH}}|^2}\right).\end{aligned}\tag{27}$$

In this paper, an explosive source is used for numerical modeling. The qSH-wave energy becomes very weak and contributes less to the ERTM image. Therefore, we combine the second and third terms in equation 27 and replace it with a curl of $\mathbf{D^P}$ as

$$\mathbf{U^P} = \mathbf{D^P}\left(\mathbf{D^P}\cdot\frac{\mathbf{U}}{|\mathbf{D^P}|^2}\right),\quad \mathbf{U^S} = -\mathbf{D^P}\times\left(\mathbf{D^P}\times\frac{\mathbf{U}}{|\mathbf{D^P}|^2}\right), \tag{28}$$

where $\mathbf{U^S} = (U_x^S, U_y^S, U_z^S)$ contains the dominant qSV-wave components and a few qSH-wave components for explosive source exploration, which can be directly used to generate the qPqS image in ERTM. Following Zhang et al. (2022), we perform a first-order Taylor expansion around $\epsilon = 0, \delta = 0$ in the denominator $1/|\mathbf{D^P}|^2$ in equation 28, which can be shown as

$$\begin{aligned}\frac{1}{|\mathbf{D^P}|^2} &= \frac{1}{k_x^2+k_y^2+a^2k_z^2}\\ &\approx \frac{1}{k_x^2+k_y^2+k_z^2} + \frac{k_z^2}{(k_x^2+k_y^2+k_z^2)^2}\cdot\frac{2v_p^2(2\epsilon-\delta)}{v_p^2-v_s^2}.\end{aligned} \tag{29}$$

Substituting equation 29 into equation 28 and converting it to the space domain, we obtain the decouple formulations of P/S waves as

$$\begin{aligned}\mathbf{u^p} &= \nabla^d(\nabla^d\cdot\mathbf{w}),\\ \mathbf{u^s} &= -\nabla^d\times(\nabla^d\times\mathbf{w}),\end{aligned} \tag{30}$$

with

$$\begin{aligned}\mathbf{w} = &-\mathrm{FFT}^{-1}\left[\frac{\mathbf{U}}{k_x^2+k_y^2+k_z^2}\right]\\ &-\mathrm{FFT}^{-1}\left[\frac{k_z^2\mathbf{U}}{(k_x^2+k_y^2+k_z^2)^2}\right]\cdot\frac{2v_p^2(2\epsilon-\delta)}{v_p^2-v_s^2},\end{aligned} \tag{31}$$

where $\nabla^d = [\,\partial_x \quad \partial_y \quad a\partial_z\,]^T$ is the inverse Fourier transform of $\mathbf{D^P}$. Here, FFT^{-1} is the inverse fast Fourier transform (FFT) operator, and $\mathbf{u^p} = (u_x^p, u_y^p, u_z^p)$ and $\mathbf{u^s} = (u_x^s, u_y^s, u_z^s)$ are vector qP- and qS-wavefields in the space domain. The elastic wavefield $\mathbf{U}$ in the wavenumber domain can be obtained by performing FFT on space domain elastic wavefields $\mathbf{u} = (u_x, u_y, u_z)$ and then substituted into equations 30 and 31 for the VTI P/S wavefields decomposition. Thus, the implementation of equations 30 and 31 requires only one forward and two inverse FFT calculations and gradient operations, which exhibit high efficiency and model adaptability in ERTM.

To summarize, a workflow chart of 3D DAS-based VTI ERTM is shown in Figure 5. When receiving the DAS records in production by using our proposed helical fiber configuration (Figure 3), those DAS responses are transformed to original seismic strain (rate) fields (using equations 13 and 18) for backward propagation in ERTM (via equation 19). Concurrently, the source wavefield is extrapolated and rebuilt by using checking point technology. The source and receiver wavefields are separated into qP- and qS-wave modes via equations 30 and 31. Finally, PP and PS images are obtained by applying dot product correlation imaging conditions (Zhang et al., 2022).

SYNTHETIC EXAMPLES

VTI layered media

To begin, we use a simple 3D VTI layered model (Figure 6) to verify the effectiveness of our proposed approach. The model size is 2000 m × 2000 m × 2000 m with a spacing step of 10 m. The flat reflector is located at a depth of 1000 m. The top layer has parameters $V_P = 2500$ m/s, $V_S = 1800$ m/s, $\rho = 2.0$, $\epsilon = 0.15$, $\delta = 0.15$, and $\gamma = 0.1$, and the bottom layer has parameters $V_P = 3000$ m/s, $V_S = 2200$ m/s, $\rho = 2.2$, $\epsilon = 0.22$, $\delta = 0.20$, and $\gamma = 0.15$. The model is smoothed by a 5 × 5 Gaussian filter.

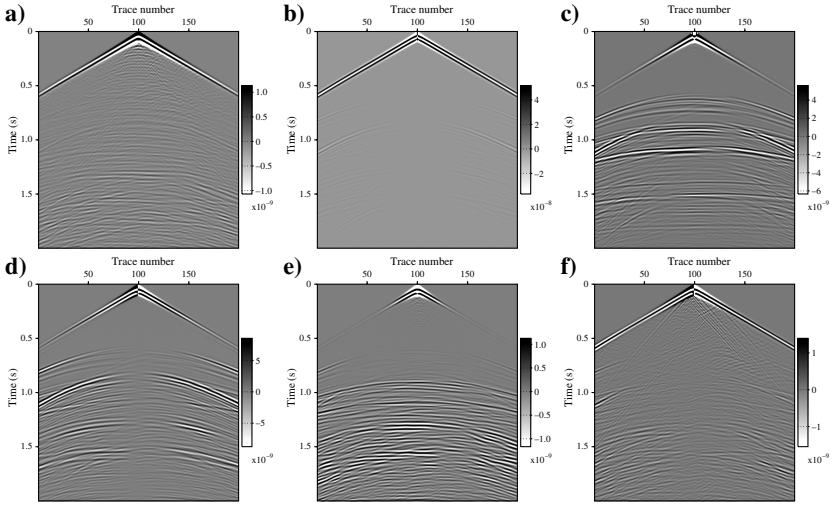

Figure 19. Reconstructed strain rate records (a) $\dot{\varepsilon}_{xx}$, (b) $\dot{\varepsilon}_{yy}$, (c) $\dot{\varepsilon}_{zz}$, (d) $\dot{\varepsilon}_{yz}$, (e) $\dot{\varepsilon}_{xz}$, and (f) $\dot{\varepsilon}_{xy}$ of the VTI arid model via equations 13 and 18 (by exchanging subscript y and z) with a gauge length of 2.45 m.

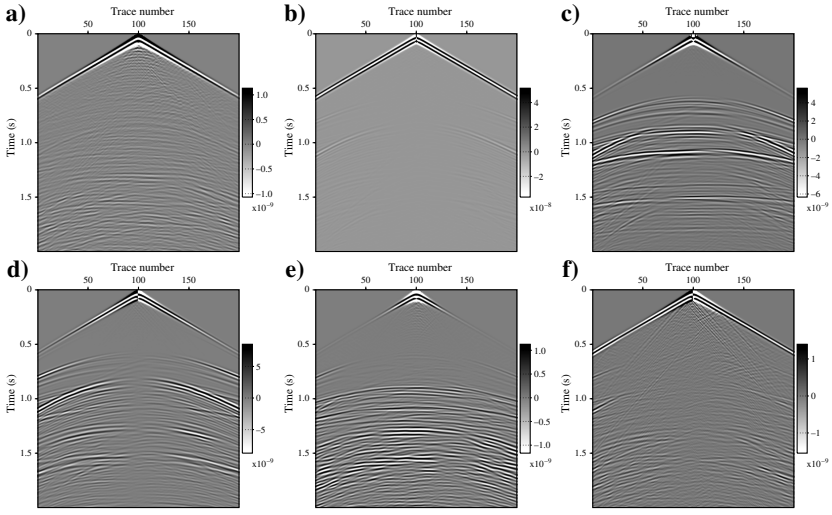

Figure 20. Reconstructed strain rate records (a) $\dot{\varepsilon}_{xx}$, (b) $\dot{\varepsilon}_{yy}$, (c) $\dot{\varepsilon}_{zz}$, (d) $\dot{\varepsilon}_{yz}$, (e) $\dot{\varepsilon}_{xz}$, and (f) $\dot{\varepsilon}_{xy}$ of the VTI arid model via equations 13 and 18 (by exchanging subscript x and z) with a gauge length of 6.05 m.

A 20 Hz Ricker wavelet is used as an explosive source with a time interval of 1 ms. A single shot (the red explosion in Figure 6) is deployed at the surface with the position of (1000, 1000) m. Figure 7 represents the original elastic wavefields in the x-, y-, and z-direction, which contains direct, reflected, and transmitted qP- and qS-waves. Using our proposed decomposition approach (equations 30 and 31), the elastic wavefields are separated into qP- and qS-wave modes (Figure 8). These decoupled P/S wavefields exhibit the correct decomposed waveforms, which enables them to be applied in VTI ERTM.

To detect the seismic strain field signal, a wellbore is set in the layered model (Figure 6) at the position from (1000, 500, 0) to (1000, 500, 2000) m. Applying our proposed configuration (Figure 3), a helical fiber is deployed along the wellbore from a depth of 0 to 2000 m. The winding parameters are the same as those of the test in Figure 4 except for the gauge length set as 1.25 m ($M = 1$) and 4.85 m ($M = 5$). According to the value of N ($N = 1$ in the test of Figure 4), a total of six 2π winding periods are required for six sampling points. In terms of these parameters, the straight distance of the six winding periods for the six sampling points is approximately 3 m, which is significantly less than the spacing interval of the layered model. Therefore, 200 receivers can be placed at each grid point along the wellbore with a spatial step of 10 m. Every trace from the receiver can be reconstructed by every group of six sampling points. By using the transformation of equation 19, we first simulate the exact strain rate records as the correct reference (Figure 9). The DAS responses are generated via equations 12 and 18. Figures 10 and 11 are the reconstructed strain rate records via our proposed helical fiber configuration (equations 13 and 18) with a gauge length of 1.25 m ($M = 1$) and 4.85 m ($M = 5$). These records illustrate qualified recovered effects compared with Figure 9. Furthermore, single trace data are extracted at the position of trace number = 50 from Figures 9–11 for amplitude comparison (Figure 12). As observed, the reconstructed strain rate data (the blue and black lines) show good agreement with the original components (the red lines), which demonstrates the effectiveness of our proposed approach.

To test the robustness of our configuration, we add random noise in the DAS records of the layer model within its data frequency band. Therefore, the areas with less useful signals are dominated by the noise. The numerical parameters remain unchanged from those in Figure 10. Figure 13 presents the recovered strain rate records from the noisy DAS data. These results are contaminated by the random noise but still keep the correct useful waveform information. Moreover, the added noise (Figure 14) is extracted from the difference between the original strain records (Figure 9) and reconstructed strain records (Figure 13). These pure noise data demonstrate that no useful information is lost in our reconstruction (Figure 13). However, we only show the recovered strain records with a small gauge length (GL = 1.25 m) in the noisy data. The reconstruction results with large gauge lengths are not exhibited because they are fully covered by noise due to the large condition number.

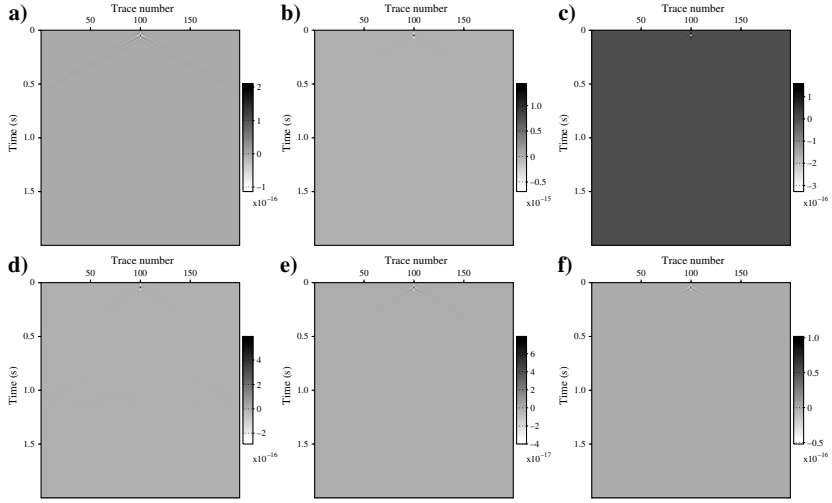

Figure 21. Difference between the exact (Figure 18) and reconstructed (Figure 19) strain rate records (a) $\dot{\varepsilon}_{xx}$, (b) $\dot{\varepsilon}_{yy}$, (c) $\dot{\varepsilon}_{zz}$, (d) $\dot{\varepsilon}_{yz}$, (e) $\dot{\varepsilon}_{xz}$, and (f) $\dot{\varepsilon}_{xy}$ with a gauge length of 2.45 m.

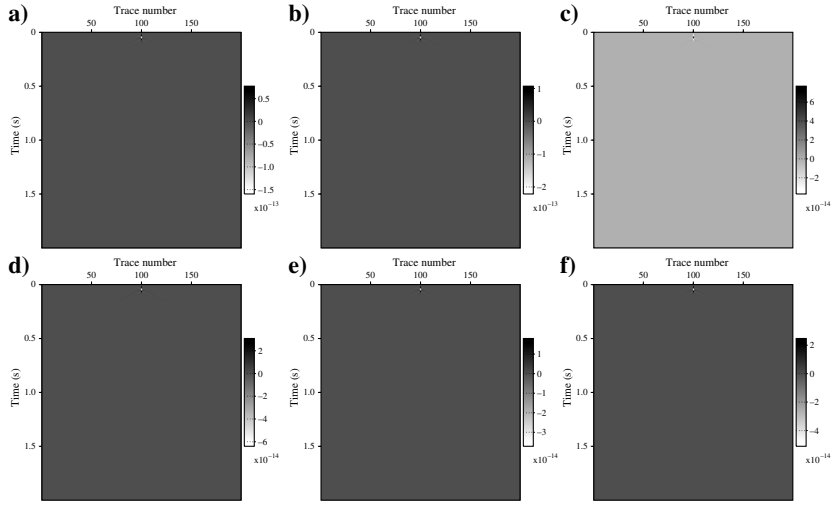

Figure 22. Difference between the exact (Figure 18) and reconstructed (Figure 21) strain rate records (a) $\dot{\varepsilon}_{xx}$, (b) $\dot{\varepsilon}_{yy}$, (c) $\dot{\varepsilon}_{zz}$, (d) $\dot{\varepsilon}_{yz}$, (e) $\dot{\varepsilon}_{xz}$, and (f) $\dot{\varepsilon}_{xy}$ with a gauge length of 6.05 m.

VTI arid model

The VTI arid model (Oristaglio, 2015) (Figure 15) is adopted as a complicated example to validate the effectiveness of our method and produce ERTM images. The model is discretized with a grid size of $200 \times 200 \times 200$ and a spacing interval of 10 m. The 20 Hz Ricker wavelet is selected as the explosive source with a sampling interval of 1 ms. A Gaussian filter with a size of 5×5 is applied for the smoothing model. A single shot is placed at the surface of (1000, 1000, 0) m for the P/S wavefields decomposition and strain component reconstruction. Figure 16 shows the

DOI:10.1190/geo2023-0354.1

elastic vector wavefields projecting on x-, y- and z-directions at a propagating speed of 1.0 s. By using our decoupled P/S approach (equations 30 and 31), the original elastic wavefields are decomposed into vector qP- and qS-wavefields (Figure 17). Because we apply an explosive source, the qS-wavefields dominate with qSV-wave components. Compared with Figure 16, these separated wavefields are qualified to suppress the cross-talk artifacts in ERTM imaging.

Different from the vertical wellbore set in a layered model (Figure 6), we bury the helical fiber at a depth of 10 m from (1000, 0, 10) to (1000, 2000, 10) to simulate the surface records. The parameters related to helical fiber are the same as those of the layered model except for the gauge length. As mentioned in the last section, the projecting matrix for the helical fiber deployed at the surface (corresponding to a 90° rotation of the wellbore in Figure 3) can be easily obtained by exchanging the subscript x (or y) with z in equation 18. Here, 200 receivers are set in the line (1000, 0, 10) to (1000, 2000, 10) with a spacing of 10 m for generating exact strain records. Figure 18 is the exact strain rate recorded by using the first-order stress-velocity wave equation and equation 19. Using our proposed helical fiber winding configuration, Figures 19 and 20 exhibit reconstructed strain components with a gauge length of 2.45 m (M = 2) and 6.05 m (M = 6), respectively. These recovered images are identical to those of Figure 18, which indicates the effectiveness of our approach in complex models. Furthermore, we also show the difference between the original strain records (Figure 18) and the reconstructed strain data (Figures 19 and 20) in Figures 21 and 22 with the same order of amplitude. As observed, there is no useful information lost during the reconstruction.

We deploy 100 shots at the surface from (1000, 0, 0) to (1000, 2000, 0) m with a spacing of 10 m for ERTM imaging. According to our proposed DAS-ERTM workflow (Figure 5), Figure 23a and 23b represents PP and PS images with the reconstructed strain field data via the proposed helical fiber configuration. Because we only deploy the helical fiber and shots in the y-direction (inline direction), the yoz-plane presents a better image than the xoz-plane. Because the explosive source is used for images, the PP-reflection energy is dominant in the strain records. As a result, the PP image (Figure 23a) exhibits a higher signal-to-noise ratio than the PS image (Figure 23b). However, the PS image possesses better resolution owing to the smaller wavelength of converted PS waves. In addition, we use the geophone data (particle velocity records) to generate PP and PS images (Figure 23c and 23d). These images using these two types of acquisition data show an analogous imaging effect. Furthermore, single trace data that are extracted from Figure 23 at x = 1500 m and y = 600 m are shown in Figure 24. By comparison, they exhibit a good accordance, which demonstrates the effectiveness and robustness of our approach.

DISCUSSION

To begin, this paper proposes a 3D efficient anisotropic P/S decomposition approach that is implemented in the space-wavenumber domain and only requires three FFTs. Although our approach shows a good performance on the decoupling P/S wave-mode, some deficiencies are worth mentioning. The polarization vectors of qP-, qSV-, and qSH-waves are derived from the 3D VTI Christoffel equation under the elliptical assumption. However, in some strong nonellipse regions, our method may encounter some artifacts. The error analysis for the ellipse media can be found in Zhang et al. (2022) and Yang et al. (2019). Concurrently, the decoupled formulation is also derived with a local homogeneous assumption. Hence, a smoothing model is recommended for the decomposing P/S wavefields in VTI ERTM. In addition, we use the explosive source to simulate the elastic wave propagation, which contains very weak qSH-wave components. Thus, we can use the curl operator (equation 28) to calculate the qSV-waves. However, when adopting

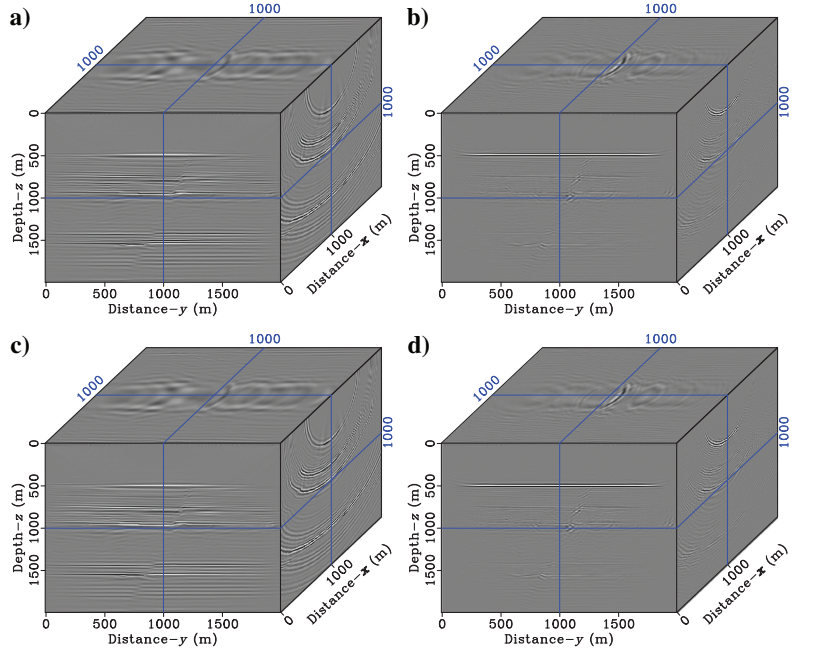

Figure 23. The ERTM images of the 3D arid model via different acquisition data. (a and b) The PP and PS image, respectively, produced with the DAS-based reconstructed data. (c and d) The PP and PS image, respectively, generated via the geophone data.

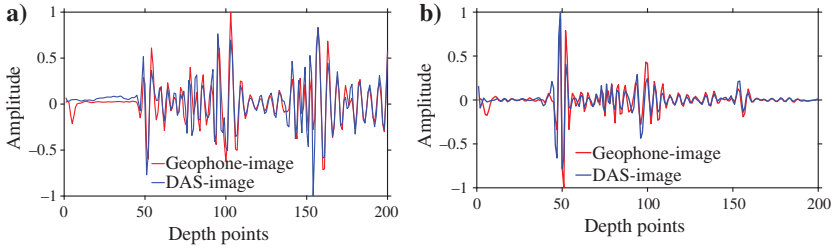

Figure 24. Comparison of single trace data extracted from Figure 23 at x = 1500 m and y = 600 m. (a) The PP data chosen from Figure 23a and 23b, and (b) the PS data selected from Figure 23c and 23d. The red lines represent the image via geophone records, and the blue lines show the image using DAS records.

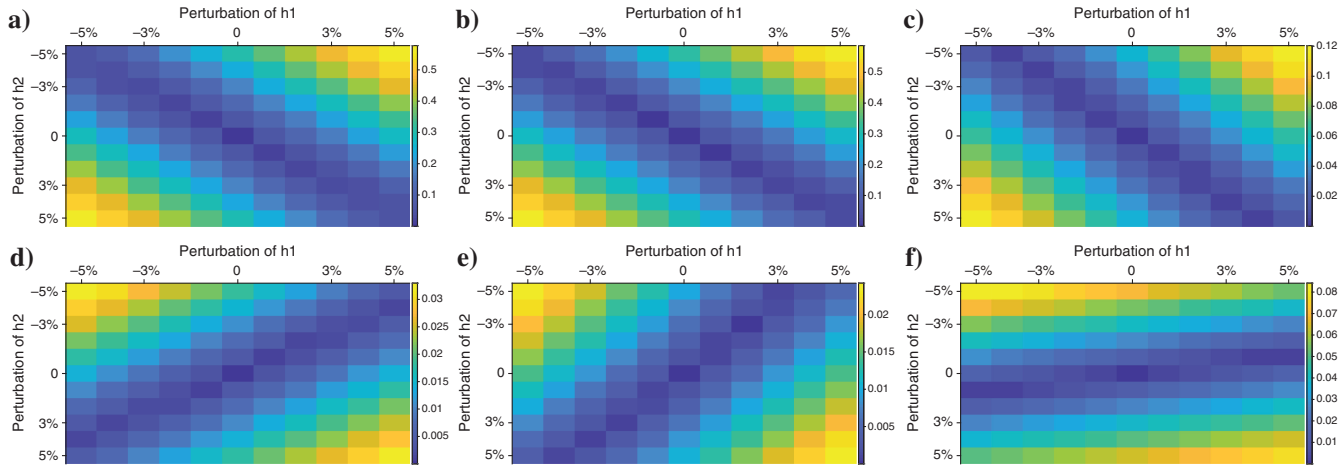

Figure 25. The relative error rate e_r of reconstructed strain components (a) ε_{xx}, (b) ε_{yy}, (c) ε_{zz}, (d) ε_{yz}, and (e) ε_{xz}, and (f) ε_{xy} with [−5% 5%] perturbations of heights $h1, h2$.

other types of sources, such as shear wave sources, the qS-wave in equations 30 and 31 includes strong qSH-waves, which may cause cross-talk artifacts.

To solve the singular projecting matrix problem of the conventional helical fiber configuration, this paper develops a nonregular variant pitch-angle winding design for the helical fiber DAS response for strain field reconstruction. In our winding configuration, the condition number of the projecting matrix is low enough to recover the original seismic strain components. However, the DAS IO instrument usually includes spatial sampling interval s and gauge length GL set. This means that we need to first estimate those two parameters and then set the pitch angles α_1 and α_2, winding radius r, M, and N in the field exploration. In this situation, the pitch angles α_1 and α_2 tend to be decimal rather than integer, such as $\alpha_1 = 66.88°$, $\alpha_2 = 53.91°$ in our numerical test. This is difficult to perform accurately in the field experiment and may cause some errors. A convenient way to tackle this problem is to use heights $h1, h2$ as marks to wind the helical fiber rather than pitch angles. However, in production, it may not achieve the accurate $h1, h2$ given in the preceding examples. Therefore, we analyze the recovery effect of strain field with ±5% perturbation range of given heights in the layered model test. All the other numerical parameters remain unchanged. The received DAS records are generated by equation 12 with the inaccurate $h1, h2$ (actual parameters), and the reconstructed strain fields components are produced from equation 25 with the accurate $h1, h2$ (ideal parameters). A relative error rate factor e_r is used for estimating the recovery accuracy and can be expressed as

$$e_r = \frac{\sum_{i=0}^{N} |\varepsilon_i - \varepsilon_i'|}{\sum_{j=0}^{N} |\varepsilon_i|}, \tag{32}$$

where ε_i and ε_i' represent the exact and reconstructed strain records, respectively. Here, N is the total number of grid points in the strain records profile. Figure 25 shows the relative error rate e_r of the reconstructed strain field components from the layer model with different perturbations of heights $h1, h2$. As observed, with similar perturbations of heights $h1, h2$, the e_r of the normal strain (Figure 25a–25c) is low and less than 3%. In the areas with largely different perturbations between $h1$ and $h2$, the e_r becomes very strong (more than 50%). The e_r of shear strain components (Figure 25d–25f) exhibits an opposite tendency to those of the normal strain components. However, the maximum of the shear strain e_r is lower than 8%, which can be acceptable for reconstruction. Those results can be a reference factor for field operation. In addition, the strain field reconstruction is conducted based on the assumption that seismic wavelengths are larger than the window length of six sampling points in helical fiber. One should be careful to set the spatial interval s and gauge length GL to fulfill that assumption.

We apply the strain field reconstructed from the helical fiber DAS response to the 3D VTI ERTM. Different than velocity records from geophones, the strain or strain rate records require the transformation of equation 19. Hence, compared with the three components of particle velocity, the six components of the strain rate field may cause more artifacts in the backward modeling of the anisotropic receiver wavefields. Decomposing these strain components into P/S wavemode in the data domain, which can further suppress the artifacts and improve the image quality for 3D VTI ERTM, is desired for the future.

CONCLUSION

To solve the ill-conditioned matrix problem of conventional helical fiber configuration, we develop a nonregular variant pitch-angle winding design for the helical fiber DAS response for strain field reconstruction. In our configuration, the condition number of the projecting matrix is low enough to recover the original strain fields. The spatial sampling interval and gauge length can be arbitrary by adjusting our design parameters. Moreover, we also propose a 3D efficient P/S wave-mode decomposition method in VTI media, which can generate the P and S wavefields with correct amplitudes and phases. By applying the reconstructed strain (rate) field components and P/S decoupling approach, a DAS-based VTI ERTM workflow is built and produces PP and PS images.

DOI:10.1190/geo2023-0354.1

ACKNOWLEDGMENTS

We appreciate the help of the editors and the anonymous reviewers for their comments and suggestions. These significantly improved the quality of this paper. This study is jointly supported by the National Key Research and Development Program of China under grant 2020YFA0710604.

DATA AND MATERIALS AVAILABILITY

The data underlying this paper are available in the paper.

REFERENCES

Caldwell, J., 1999, Marine multicomponent seismology: The Leading Edge, **18**, 1274–1282, doi: 10.1190/1.1438198.

Chen, K., and M. D. Sacchi, 2017, Elastic least-squares reverse time migration via linearized elastic full-waveform inversion with pseudo-Hessian preconditioning: Geophysics, **82**, no. 5, S341–S358, doi: 10.1190/geo2016-0613.1.

Cheng, J., and S. Fomel, 2014, Fast algorithms for elastic-wave-mode separation and vector decomposition using low-rank approximation for anisotropic media: Geophysics, **79**, no. 4, C97–C110, doi: 10.1190/geo2014-0032.1.

Dellinger, J., and J. Etgen, 1990, Wavefield separation in two-dimensional anisotropic media: Geophysics, **55**, 914–919, doi: 10.1190/1.1442906.

Dou, S., N. Lindsey, A. M. Wagner, T. M. Daley, B. Freifeld, M. Robertson, J. Peterson, C. Ulrich, E. R. Martin, and J. B. Ajo-Franklin, 2017, Distributed acoustic sensing for seismic monitoring of the near surface: A traffic-noise interferometry case study: Scientific Reports, **7**, 11620–11633, doi: 10.1038/s41598-017-11986-4.

Eaid, M. V., S. D. Keating, and K. A. Innanen, 2020, Multiparameter seismic elastic fullwaveform inversion with combined geophone and shaped fiber-optic cable data: Geophysics, **85**, no. 6, R537–R552, doi: 10.1190/geo2020-0170.1.

Egorov, A., J. Correa, A. Bna, R. Pevzner, K. Tertyshnikov, S. Glubokovskikh, V. Puzyrev, and B. Gurevich, 2018, Elastic full-waveform inversion of vertical seismic profile data acquired with distributed acoustic sensors: Geophysics, **83**, no. 3, R273–R281, doi: 10.1190/geo2017-0718.1.

Granli, J. R., B. Arntsen, A. Sollid, and E. Hilde, 1999, Imaging through gas-filled sediments using marine shear-wave data: Geophysics, **64**, 668–677, doi: 10.1190/1.1444576.

Innanen, K., 2017, Determination of seismic-tensor strain from helical wound cable- distributed acoustic sensing cable with arbitrary and nested-helix winds: 87th Annual International Meeting, SEG, Expanded Abstracts, 926–930, doi: 10.1190/segam2017-17664060.1.

Lindsey, N. J., H. Rademacher, and J. B. Ajo-Franklin, 2020, On the broadband instrument response of fiber-optic das arrays: Journal of Geophysical Research: Solid Earth, **125**, 1–16, doi: 10.1029/2019JB018145.

Liu, L., 2019, Improving seismic image using the common-horizon panel: Geophysics, **84**, no. 5, S449–S458, doi: 10.1190/geo2018-0656.1.

Liu, L., R. Ding, H. Liu, and H. Liu, 2015, 3D hybrid-domain full waveform inversion on GPU: Computers and Geosciences, **83**, 27–36, doi: 10.1016/j.cageo.2015.06.017.

Lo, T. W., and P. L. Inderwiesen, 2012, Fundamentals of seismic tomography: SEG Books.

Mateeva, A., J. Lopez, H. Potters, J. Mestayer, B. Cox, D. Kiyashchenko, P. Wills, S. Grandi, K. Hornman, B. Kuvshinov, W. Berlang, Z. Yang, and R. Detomo, 2014, Distributed acoustic sensing for reservoir monitoring with vertical seismic profiling: Geophysical Prospecting, **62**, 679–692, doi: 10.1111/1365-2478.12116.

Ning, I. L. C., and P. Sava, 2018a, High-resolution multi-component distributed acoustic sensing: Geophysical Prospecting, **66**, 1111–1122, doi: 10.1111/1365-2478.12634.

Ning, I. L. C., and P. Sava, 2018b, Multicomponent distributed acoustic sensing: Concept and theory: Geophysics, **83**, no. 2, P1–P8, doi: 10.1190/geo2017-0327.1.

Ning, I. L. C., and P. Sava, 2018c, Multicomponent imaging with distributed acoustic sensing: 88th Annual International Meeting, SEG, Expanded Abstracts, 4683–4687, doi: 10.1190/segam2018-2997182.1.

Oristaglio, M., 2015, SEAM update: The Leading Edge, **34**, 466–468, doi: 10.1190/tle34040466.1.

Ren, Z., and Y. Liu, 2015, Elastic full-waveform inversion using the second-generation wavelet and an adaptive-operator-length scheme: Geophysics, **80**, no. 4, R155–R173, doi: 10.1190/geo2014-0516.1.

Tang, J., H. Yue, X. Xiangrong, J. Tinnin, and J. Hallin, 2009, Application of converted-wave 3D/3-C data for fracture detection in a deep tight-gas reservoir: The Leading Edge, **28**, 826–837, doi: 10.1190/1.3167785.

Tsvankin, I., 2012, Seismic signatures and analysis of reflection data in anisotropic media, 3rd ed.: SEG.

Wang, W., B. Hua, G. A. McMechan, and B. Duquet, 2018, P- and S-decomposition in anisotropic media with localized low-rank approximations: Geophysics, **83**, no. 1, C13–C26, doi: 10.1190/geo2017-0138.1.

Willis, M. E., 2022, Distributed acoustic sensing for seismic measurements — What geophysicists and engineers need to know: SEG.

Yan, J., and P. Sava, 2009, Elastic wave-mode separation for VTI media: Geophysics, **74**, no. 5, WB19–WB32, doi: 10.1190/1.3184014.

Yang, J., H. Zhang, Y. Zhao, and H. Zhu, 2019, Elastic wavefield separation in anisotropic media based on eigenform analysis and its application in reverse-time migration: Geophysical Journal International, **217**, 1290–1313, doi: 10.1093/gji/ggz085.

Zhan, G., and J. Nahm, 2020, Multi-well 3D DAS VSPs: Illumination and imaging beyond the wellbores: 90th Annual International Meeting, SEG, Expanded Abstracts, 3798–3802, doi: 10.1190/segam2020-3426032.1.

Zhang, L., L. Liu, F. Niu, J. Zuo, D. Shuai, W. Jia, and Y. Zhao, 2022, A novel and efficient engine for P/S wave-mode vector decomposition for VTI elastic reverse time migration: Geophysics, **87**, no. 4, S185–S207, doi: 10.1190/geo2021-0609.1.

Zhang, Q., and G. A. McMechan, 2010, 2D and 3D elastic wavefield vector decomposition in the wavenumber domain for VTI media: Geophysics, **75**, no. 3, D13–D26, doi: 10.1190/1.3431045.

Zhao, Y., H. Zhang, H. Liu, D. Zhang, and M. Sengupta, 2018, Target-oriented diversity stacking for virtual-source imaging and monitoring: The Leading Edge, **37**, 764–773, doi: 10.1190/tle37100764.1.

Zuo, J., F. Niu, L. Liu, S. Da, H. Zhang, J. Yang, L. Zhang, and Y. Zhao, 2022, 3D anisotropic P- and S-mode wavefields separation in 3D elastic reverse-time migration: Surveys in Geophysics, **43**, 673–701, doi: 10.1007/s10712-021-09688-8.

Biographies and photographs of the authors are not available.